Modeling Interference for the Coexistence of 6G Networks and Passive Sensing Systems

Paolo Testolina[®], *Member, IEEE*, Michele Polese[®], *Member, IEEE*, Josep Miquel Jornet[®], *Fellow, IEEE*, Tommaso Melodia[®], *Fellow, IEEE*, and Michele Zorzi[®], *Fellow, IEEE*

Abstract—Future wireless networks and sensing systems will benefit from access to large chunks of spectrum above 100 GHz, to achieve terabit-per-second data rates in 6th Generation (6G) cellular systems and improve accuracy and reach of Earth exploration and sensing and radio astronomy applications. These are extremely sensitive to interference from artificial signals, thus the spectrum above 100 GHz features several bands which are protected from active transmissions under current spectrum regulations. To provide more agile access to the spectrum for both services, active and passive users will have to coexist without harming passive sensing operations. In this paper, we provide the first, fundamental analysis of Radio Frequency Interference (RFI) that large-scale terrestrial deployments introduce in different satellite sensing systems now orbiting the Earth. We develop a geometry-based analysis and extend it into a data-driven model which accounts for realistic propagation, building obstruction, ground reflection, for network topology with up to 10⁵ nodes in more than 85 km². We show that the presence of harmful RFI depends on several factors, including network load, density and topology, satellite orientation, and building density. The results and methodology provide the foundation for the development of coexistence solutions and spectrum policy towards 6G.

Index Terms— Coexistence, passive sensing, 6th Generation (6G), terahertz (THz), sub-terahertz (sub-THz).

I. INTRODUCTION

ONTINUOUSLY growing user demand is pushing the 6th Generation (6G) of wireless networks into the subterahertz (sub-THz) spectrum of 100-300 GHz [1]. The sub-THz spectrum offers theoretically orders of magnitude greater bandwidth than typical communication bands depending on the composition of the atmosphere and weather conditions [2]. This makes sub-THz attractive for wireless networks, despite

Manuscript received 25 July 2023; revised 16 November 2023; accepted 17 January 2024. Date of publication 7 February 2024; date of current version 14 August 2024. This work was supported in part by NSF under Award CNS-2225590 and Award CNS-2332721. The work of Paolo Testolina was supported by Fondazione CaRiPaRo through "Dottorati di Ricerca" 2019. The associate editor coordinating the review of this article and approving it for publication was M. Wang. (Corresponding author: Michele Polese.)

Paolo Testolina was with the Department of Information Engineering, University of Padova, 35131 Padua, Italy. He is now with Northeastern University, Boston, MA 02115 USA (e-mail: testolina@dei.unipd.it).

Michele Zorzi is with the Department of Information Engineering, University of Padova, 35131 Padua, Italy (e-mail: zorzi@dei.unipd.it).

Michele Polese, Josep Miquel Jornet, and Tommaso Melodia are with the Institute for the Wireless Internet of Things, Northeastern University, Boston, MA 02115 USA (e-mail: m.polese@northeastern.edu; j.jornet@northeastern.edu; melodia@northeastern.edu).

Color versions of one or more figures in this article are available at https://doi.org/10.1109/TWC.2024.3360628.

Digital Object Identifier 10.1109/TWC.2024.3360628

the significant challenges related to blockage, low transmission power, and small antenna apertures, which require directional antennas to increase the Next Generation Node Base (gNB) coverage [3].

However, this portion of the spectrum is already used by remote (passive) sensing systems in Earth Exploration-Satellite Service (EESS) and radio astronomy, supporting the weather, climate, and astronomy enterprises. Such services can tolerate limited to no interference. For this reason, the spectrum above 100 GHz features a set of channels reserved for passive remote sensing. This results in 12.5 GHz being the largest contiguous bandwidth available for communications under 200 GHz under current spectrum regulations [4]. Without sharing portions of the spectrum between EESS and the sub-THz terrestrial communication systems, there is little benefit in climbing all the way from 71 GHz into sub-THz or terahertz (THz) bands, if the resulting bandwidth will be comparable. Hence, channels wider than 12.5 GHz are very much desired. Further, larger chunks of microwave and sub-THz spectrum can also benefit passive sensing systems themselves, e.g., for more precise hyper-spectral remote sensing [5]. The same applies to radio astronomy, to sense molecular shifts in bands outside those traditionally allocated for this use [4].

Therefore, today's fixed spectrum allocation is limiting the potential of both communications and remote sensing. While this could be true across the entire radio spectrum, the much more challenging propagation of sub-THz and THz signals through the atmosphere and the opportunity to more precisely control the radiation with compact antenna structures opens the door to more flexible spectrum sharing strategies [4], [6], [7]. To date, however, the literature presents a gap in the modeling and analysis of the Radio Frequency Interference (RFI) caused by terrestrial next-generation wireless networks to EESS systems, as most analyses focus on single-link evaluations, simplified terrestrial network models, and tractable but simplified channel models [4], [7]. Modeling RFI is key to the development of tailored coexistence techniques. This is a timely need for the passive sensing and sub-THz networking communities, as RFI insights can influence 6G standardization and next generations of remote sensing systems, allowing coexistence embedded in the technology rather than layered on top as an afterthought.

A. Contributions

In this paper, we fill this gap with the first analysis of 6G terrestrial RFI to passive sensing systems. We combine

1536-1276 © 2024 IEEE. Personal use is permitted, but republication/redistribution requires IEEE permission. See https://www.ieee.org/publications/rights/index.html for more information.

a tractable yet simplified analytical model with a large-scale simulation study. The first highlights the dynamics and interactions among directional communications in the terrestrial network, ground reflections, satellite orbit and sensor orientation, and propagation at sub-THz frequencies. It shows that using narrow beams is not enough to protect from RFI. The simulations build on such insights to numerically evaluate RFI in a variety of large-scale scenarios, using models for networks with up to 10^5 nodes in more than $85~\rm km^2$ and actual sensors deployed on multiple EESS missions. Our contributions are as follows:

- In both analysis and simulation, we model the channel with aggregated interference, ground reflections, terrestrial and EESS sensors beam patterns, building obstructions, and sub-THz spreading and absorption losses, extending ITU models with deployment-specific details. Our model is extremely scalable and can also be used to analyze and model Non Terrestrial Networks (NTNs)
- We analyze the single-link interference probability, and show how the peculiar geometry of the terrestrial-satellite RFI setup can lead to significant interference from the ground reflection due to the combination of the terrestrial and satellite beam gains.
- We extend this into a data-driven large-scale simulation with multiple satellites (i.e., TEMPEST-D and the Microwave Limb Sounder (MLS) [8], [9]) and device deployments and obstructions based on OpenStreetMap (OSM) and 3D models, including urban cellular and backhaul. The area size and the number of buildings (62512 3D polygons) are unprecedented and showcase how we can model large-scale, site-specific deployments.
- We show that dense sub-THz networks can affect EESS satellites operations. Specifically, (i) even User Equipments (UEs) can generate harmful interference, when combined in large numbers; (ii) the secondary reflections (e.g., the ground reflection), although generating lower interference, are significant and not to be neglected; (iii) the attenuation outside the main lobe of directional arrays might not be enough to protect the passive users; whereas (iv) path loss and atmospheric attenuation as well as the building obstruction can shield them more effectively.

Therefore, there exist regimes in which interference is significant, and other conditions in which it does not lead to any harm to passive satellites. These insights are a starting point for (i) the design of 6G networks; (ii) passive/active sharing, based on an accurate RFI understanding; and (iii) data-driven spectrum policy toward 6G.

II. RELATED WORKS

RFI analyses follow two main approaches. Single-link analysis considers the RFI generated by a single interferer and a single victim [4], [7], [10], [11]. Specifically, [12] was among the first studies to numerically characterize RFI at sub-THz frequencies. Reference [4] analyzes it in several scenarios for a single backhaul, terrestrial link. Similarly, [7] considers an urban scenario where a receiver on a rooftop is used as a surrogate for the satellite. The overall attenuation is measured

for different ground transmitter locations. The authors of both studies conclude that, for a single link in an urban area, harmful interference can be avoided if the satellite or the beam direction remains below certain angles.

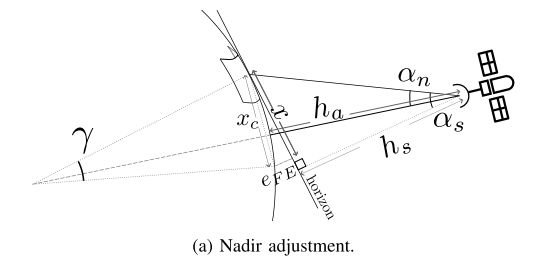
The second approach relies on Monte Carlo simulations to aggregate interference from multiple interferers modeled through multiple random variables. RFI statistics are derived through multiple iterations. References [13] and [14] consider a Fixed Satellite Service (FSS) terrestrial station and compute the aggregated interference produced by the gNBs of a nearby network at 3.4-3.6 GHz and 18 GHz. The authors of [15] analyze the impact of automotive radars on satellite radiometers in the 22-27 GHz frequency range, and conclude that most realistic vehicle densities would generate harmful RFI. The authors of both studies conclude that coexistence between the two systems at millimeter wave (mmWave) frequencies is possible, provided that the base station deployment and configuration respect some conditions. References [13], [16], and [17] consider random deployments of the gNBs and UEs, realistic antenna and beamforming radiation patterns, and stochastic channel models [18]. Reference [19] provides an analysis of the interference between terrestrial and satellite relays in the 25.25-27.5 GHz bands, considering Line-of-Sight (LoS) propagation and the ITU channel model, and aggregating the interference over extremely wide areas $(0.5^{\circ} \times 0.5^{\circ} \text{ latitude/longitude})$. The authors of [20] estimate the aggregated RFI distribution from a Fast Switching (FS) network to an aircraft at 18 GHz. In [21], [22], and [23], the coexistence between terrestrial networks and EESS at mmWave frequencies is analyzed. Finally, obstruction by physical obstacles is modeled in [24], where the authors stochastically estimates the aggregated interference from a wide area for the upper 6 GHz band using building statistics from real data for the city of Milan. Compared to prior literature, this paper combines a tractable analytical model, to intuitively illustrate the combined effect of ground reflections, directional communications, and the sub-THz channel on RFI, and simulations that numerically profile RFI at an unprecedented scale, considering a realistic topology rather than random variables for beam orientation and blockage.

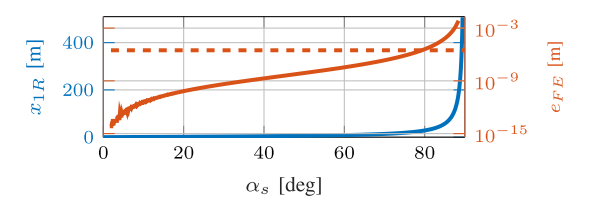
III. PROPAGATION MODEL

In this section, we extend the channel models from [25] and [26] to improve their scalability and to embed key elements of propagation at frequencies above 100 GHz. We model the propagation through two paths: the direct or LoS ray and the ray reflected by the ground (Ground Reflection (GR)), to provide key insights on the multipath contribution to the overall RFI at the satellite. Thus, the ray power takes into account (a) the reflection loss (for the reflected ray); (b) the free-space spreading loss; (c) the "atmospheric" loss due to the molecular absorption of the atmosphere layers crossed by the ray; and (d) the absorption loss due to obstacles.

A. Ground-to-Satellite Path

The traditional 2-ray model [25] is based on the flat-Earth assumption when considering short distances. The effect of





(b) 2D-distance from the ground node to the reflection point (blue) and corresponding flat-Earth approximation error (orange) for different look-angles for a satellite at $400~\rm km$ altitude and a ground node at $10~\rm m$ from the ground.

Fig. 1. Schematic representation of the geometry of the system (a) and error due to the flat-Earth approximation (b).

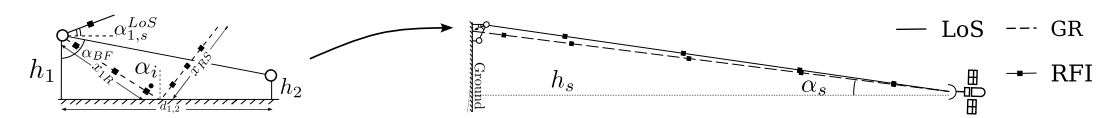


Fig. 2. Geometry of the problem (not to scale).

this simplification has been evaluated in several works [27], [28], [29], [30], [31]. However, the distance between the satellite and the ground node can be hundreds of kilometers not only on the altitude but also on the longitudinal plane. Here, we verify whether the flat-Earth assumption holds when considering the path reflected on the ground from the terrestrial node to the satellite.

Consider a satellite at altitude h_a , which points the main lobe of its sensor towards the ground with an angle α_n with respect to nadir. By definition, the nadir at a given point is the direction pointing toward the center of the Earth. As shown in Fig. 1a, we distinguish between the *nadir* angle α_n , i.e., the angle between the pointing direction and nadir, and the apparent nadir angle α_s seen from the ground, i.e., the angle between the pointing direction of the satellite and the normal to the horizon. The relation between the two angles can be expressed as [32]

$$\alpha_s = \arcsin\left(\frac{r}{R}\sin\alpha_n\right),\tag{1}$$

where R is the Earth radius and $r=R+h_a$ is the distance of the satellite from the center of the Earth, here assumed to be a perfect sphere for simplicity. Thus, a satellite at the horizon, with $\alpha_s=90^\circ$, has a nadir angle $\alpha_n=\arcsin\left(\frac{R}{r}\right)$, that for a satellite at $h_a=400$ km of altitude corresponds to about 70.21° . Conversely, the same satellite looking at a 65° angle with respect to nadir has an apparent look-angle $\alpha_s=74.41^\circ$.

From α_s it is straightforward to derive the incidence angle α_i , the LoS angle $\alpha_{1,s}^{LoS}$ between the ground node and the satellite, the distance x_{1R} (x_{RS}) between the ground node (satellite) and the reflection point, and the overall length of the reflected path x:

$$\alpha_i = \arctan\left(\frac{h_s}{h_s + h_1} \tan \alpha_s\right) \simeq \alpha_s$$
 (2)

$$\alpha_{1,s}^{LoS} = \arctan\left(\frac{h_s - h_1}{(h_s + h_1)\tan\alpha_i}\right) + \frac{\pi}{2}$$
 (3)

$$\simeq \arctan\left(\frac{1}{\tan \alpha_s}\right) + \frac{\pi}{2} = \pi - \alpha_s$$
 (4)

$$x_{1R} = h_1 \tan \alpha_i$$
 $x_{RS} = h_s \tan \alpha_i$

$$x_{GR} = x_{1R} + x_{RS} \tag{2}$$

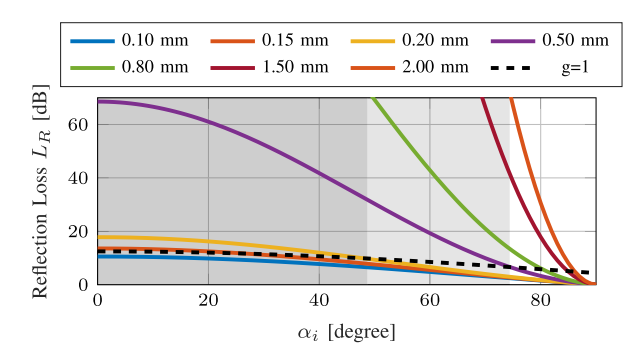
We define the flat-Earth error at distance x from node 1 as $e_{FE}(x) = |h_{FE}(x) - h_{E}(x)|$, where $h_{FE}(x)$ and $h_{E}(x)$ are the flat and spherical Earth ground height at distance x, respectively. The error can be computed as $e_{FE}(x) =$ $x^2 + x_c^2 - 2xx_c\cos\left(\frac{\gamma}{2}\right)$, where $x_c = 2R\sin\left(\frac{\gamma}{2}\right)$ and $\gamma =$ $\arctan\left(\frac{x}{R}\right)$ are defined as in Fig. 1a. Fig. 1b shows the distance x_{1R} (blue) of the reflection point from the ground node, and the corresponding flat-Earth error $e_{FE}(x_{1R})$, for a ground node at 10 m and a satellite at 400 km altitude at different look-angles α_s . Considering that at sub-THz frequencies the wavelength is in the order of millimeters, we can set 3×10^{-6} m as a threshold for the flat-Earth error, to keep the corresponding phase error below 1° for frequencies up to 300 GHz. This translates to a ground reflection point closer than 30 m from the ground node, or, correspondingly, to the satellite at about 10° above the horizon ($\alpha_s < 80^{\circ}$). For $\alpha_s > 80^{\circ}$, the reflection point is so far from the ground node that the curvature of the Earth needs to be accounted for. In that case, the approximations for the reflected path do not hold, whereas the model for the LoS remains valid. However, since in this work we are interested in analyzing also the effect of multipath, we limit our analysis to elevation angles $\alpha_s \leq 80^{\circ}$.

B. Ray Power

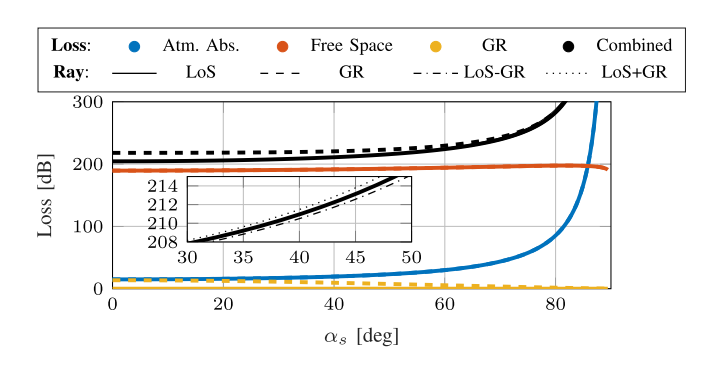
As represented in Fig. 2, in our channel model we consider the direct ray (j = 0: LoS) and the ray reflected on the ground (j = 1), representing the two main propagation paths from the source to the receiver. Each ray is associated with a path loss L_j that depends on a number of elements, detailed in the following paragraphs.

a) Reflection loss: If the ray j is reflected, a reflection loss $L_{R,j}$ is applied, which changes with the incidence angle, with the polarization of the wave, and with the material of the reflecting surface. In this paper, we consider the reflection loss presented in [26], derived from [33].

The Fresnel reflection coefficients r_{TE} and r_{TM} model the power loss in the specular direction when the wave is reflected on a smooth surface for the Transverse Electric (TE) and Transverse Magnetic (TM) polarized waves, respectively.



(a) Reflection loss L_R at 178 GHz for different values of the standard deviation σ of the surface roughness. g=1 (black dashed) marks the separation between rough and smooth surfaces, as confirmed by the much greater losses for $\sigma>0.20$ mm.



(b) Contribution of the different losses at 178 GHz for a satellite at 400 km of altitude, for different elevation angles α_s of the satellite. We report the losses applied to the LoS (solid) and reflected (dashed) ray, and the constructive and destructive combination of the two rays (dash-dotted and dotted). The free-space loss dominates, with the atmospheric absorption dominating when the satellite is at the horizon and the signal crosses a larger section of the atmosphere.

Fig. 3. Analysis of the reflection loss (a) and of the overall path loss with the individual contributions (b).

We present only the derivation for TE-polarized waves, without polarization loss, as the formulation for the TM mode is analogous. The reflection coefficient $r=r_{TE}$ can be computed, considering the refraction index n and the absorption coefficient α , as

$$r = \frac{\cos \alpha_i - n\sqrt{1 - \left(\frac{1}{n}\sin \alpha_i\right)^2}}{\cos \alpha_i + n\sqrt{1 - \left(\frac{1}{n}\sin \alpha_i\right)^2}} = |r| e^{j\phi_R}$$
 (6)

where $n=\sqrt{\epsilon}$ is the refractive index and ϕ_R is the phase shift that occurs during the reflection. Relative permittivity coefficients $\epsilon\in\mathbb{C}$ for common building materials in the frequency range of interest are reported in [34]. For simplicity, throughout this work we assume that $\phi_R=\pi$, i.e., r=-|r|.

When considering outdoor propagation, particularly at high frequencies, reflections occur on rough materials, where scattering becomes relevant. To include the scattering loss in the specular direction, we multiply the Fresnel coefficient by the Rayleigh roughness factor

$$L_{R,j} = (\rho \cdot r)^{-1}, \text{ with } \rho = e^{-\frac{g}{2}},$$
 (7)

where the roughness g of the material ($g \ll 1$: smooth, $g \simeq 1$ moderately rough, g > 1 very rough) is defined as $g = \left(\frac{4\pi\sigma\cos\alpha_i}{\lambda}\right)^2$, where σ is the standard deviation of the surface roughness [33]. Note that the dependence of g on the incident angle α_i accounts for the effective roughness seen by the incoming wave. Fig. 3a reports the reflection loss as a function of the incident angles for different values of σ , computed with the relative permittivity for the concrete $\epsilon = 5.24$ [34], that is used throughout the rest of this work.

b) Free-Space loss: As the j-th ray propagates through the space, the signal is attenuated proportionally to the distance d_j and to the center frequency f_c . The free-space loss for ray j is thus computed as

$$L_{fs,j} = \frac{4\pi f_c d_j}{c}. (8)$$

Clearly, the LoS path is the shortest, with length $d_0 < d_j$, $j \in \mathbb{N}^+$. The length difference Δd between the LoS and the

ground-reflected ray is approximated for the case of ground-to-satellite propagation in Eq. (9). An approximation for the phase difference in the two-ray model commonly adopted in the literature [25] is $\Delta d \simeq 2 \frac{h_1 h_s}{x}$, which holds when $x \gg h_1 + h_s$. However, in the considered case, this assumption is not verified, and the approximation is not valid. Thus, we derived an approximation that can be applied to satellite communications:

$$\Delta d = \sqrt{x^2 + (h_1 + h_s)^2} - \sqrt{x^2 + (h_s - h_1)^2}$$

$$= \frac{x^2 + (h_1 + h_s)^2 - (x^2 + (h_s - h_1)^2)}{\sqrt{x^2 + (h_1 + h_s)^2} + \sqrt{x^2 + (h_s - h_1)^2}}$$

$$= \frac{4h_1}{\sqrt{\left(\frac{x}{h_s}\right)^2 + \left(\frac{h_1}{h_s} + 1\right)^2} + \sqrt{\left(\frac{x}{h_s}\right)^2 + \left(1 - \frac{h_1}{h_s}\right)^2}}$$

$$= \simeq \frac{4h_1}{\sqrt{\left(\frac{x}{h_s}\right)^2 + 1} + \sqrt{\left(\frac{x}{h_s}\right)^2 + 1}}$$

$$= \frac{2h_1}{\sqrt{\left(\frac{x}{h_s}\right)^2 + 1}} = \frac{2h_1}{\sqrt{\left(\tan\left(\alpha_s\right)\right)^2 + 1}}$$
(9)

where the approximation holds for $h_s \gg h_1$, which applies to ground-to-satellite scenarios.

Fig. 3b compares the path loss of the direct and of the reflected ray. Note from Eq. (9) that Δd varies between 0 (satellite at the horizon) and $2h_1$ (satellite directly above the ground node), that makes the difference between the free-space loss of the two paths negligible.

c) Atmospheric loss: Electromagnetic waves propagating through the atmosphere interact with the molecules, transferring part of their energy to the medium. This effect is accounted for through the atmospheric absorption coefficient $L_{A,j}$, which depends on the composition of the atmospheric layers and on the propagation angle of the j-th ray [4], [6]:

$$L_{A,j} = \left(\int_0^{h_a} \frac{\gamma(h)}{\sqrt{1 - \cos^2(\theta(h))}} \, \mathrm{d}h \right)^{-1} \tag{10}$$

where $\gamma(h) = \gamma_o(h) + \gamma_w(h)$ is the attenuation given by oxygen (γ_o) and water vapor (γ_w) at height h, h_a is the satellite altitude, and $\theta(h)$ is the local apparent elevation angle at height h.

d) Absorption loss: In the sub-THz bands, the transmitted power through materials is negligible [35]. Thus, for large obstacles, e.g., buildings, with multiple, thick, non-reflective layers, a hard, on/off loss can be applied. Specifically, we model the building blockage as $L_B = +\infty$ if the ray is obstructed, or $L_B = 1$ otherwise.

Factoring in these elements, the overall loss for ray j is

$$L_{i} = L_{fs,i} L_{R,i} L_{A,i} L_{B,j}.$$
 (11)

Fig. 3b shows the different contributions to the path loss at $f_c=178~\mathrm{GHz}$ for a satellite at $400~\mathrm{km}$ of altitude, for different apparent look-angles α_s .

C. Ray Combining

Considering the propagation of a generic electric signal $E_s \in \mathbb{C}$ from the source to the receiver, the signal E at the receiver antenna is given by the superposition of the electric fields of the LoS and ground-reflected rays

$$E = \sum_{j=0,1} E_j = \left(\frac{E_s e^{j2\pi\tau_0 f_c}}{L_{B,0} L_{fs,0} L_{A,0}} + \frac{E_s e^{j2\pi\tau_1 f_c + \phi_R}}{L_{B,1} L_{fs,1} |L_R| L_{A,1}}\right)$$

$$= E_s e^{j2\pi\tau_0 f_c} \left(\frac{1}{L_{B,0} L_{fs,0} L_{A,0}} + \frac{e^{j2\pi\frac{\Delta d}{\lambda} + \phi_R}}{L_{B,1} L_{fs,1} |L_R| L_{A,1}}\right)$$

$$\simeq \frac{E_s}{L_{fs,0} L_{A,0}} e^{j2\pi\tau_0 f_c} \left(\frac{1}{L_{B,0}} + \frac{e^{j2\pi\frac{\Delta d}{\lambda} + \pi}}{L_{B,1} |L_R|}\right)$$
(12)

where $\Delta d=d_1-d_0>0$ is the difference between the length of the two paths; and f_c and $\lambda=\frac{c}{f_c}$ are the central frequency and the wavelength of the signal.

The approximations $L_{fs,0}=L_{fs,1}$ and $L_{A,0}=L_{A,1}$ are justified by the fact that for very long propagation distances, e.g., when considering the transmission from the ground to the satellite, the difference in path length Δd is small, making the atmospheric and the free-space losses experienced by the two rays almost equal. On the contrary, this kind of approximation does not hold in general for the phase. This is particularly true when considering high frequencies/short wavelengths, as the two rays are in phase opposition when $\Delta d=2k\frac{\lambda}{2}, k\in\mathbb{N}$, i.e., a path difference of $\frac{\lambda}{2}$, in the order of millimeters or less for frequencies above 100 GHz, determines whether the rays combine constructively or destructively.

IV. SINGLE LINK ANALYSIS

In this section, we present a brief geometry-based analysis of the problem, that serves as the basis for the simulation setup, considering a single terrestrial link and an incumbent EESS. We analytically demonstrate that (i) reflections play a significant role in the RFI analysis, and that (ii) narrow beams, while successfully suppressing the direct interference, might amplify the undesired interfering multipath components. With these goals in mind, we keep the assumptions purposefully ideal and the scenario simple for tractability

reasons, and to prove the main points that are observed in the realistic, yet much more complex simulations reported in Secs. V and VI.

The two factors that come into play when considering the propagation of electromagnetic waves at such high frequencies are (i) their interaction with the environment, described by the propagation model introduced in Secs. III, and (ii) the spatial distribution of the power, determined by the radiation and beamforming patterns of the antennas.

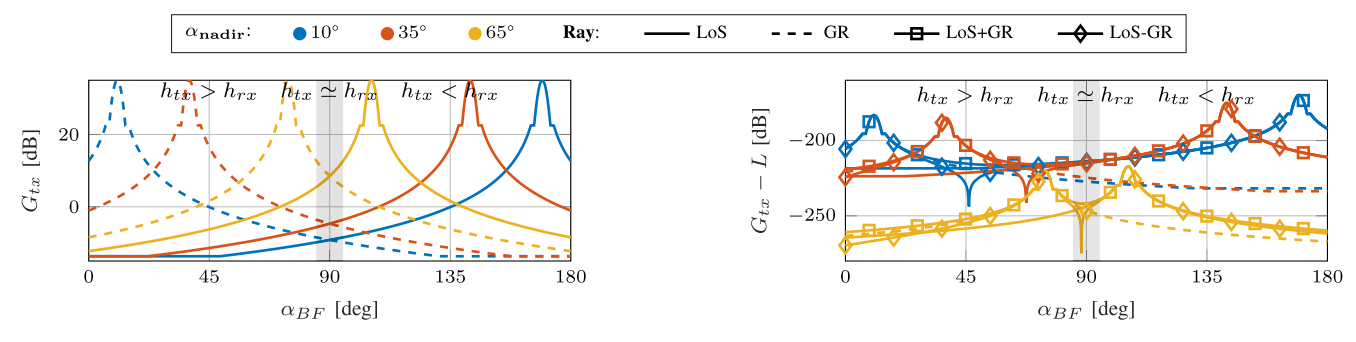
Prior work on RFI to satellite systems [4], [7] shows, often adopting a LoS channel model, that the narrow beamforming used in mmWave and sub-THz networks can reduce enough the power that leaks in the direction of the passive user so as not to cause any significant interference. However, due to the particular geometry of the ground-to-satellite interference, represented in Fig. 2, reflections can not be neglected. In this section, we start by analyzing the geometry of a single link in Sec. IV-A to show that the power received through the ground reflection—accounting for propagation and beamforming—is not negligible, and comparable to the LoS ray in some cases. We then derive the corresponding probabilities for a single link in Sec. IV-B, and provide some considerations on the impact of the frequency band in Sec. IV-C.

A. Beamforming Amplification

Consider the link between a Transmitter (TX) and a Receiver (RX) with heights h_{tx} and h_{rx} , respectively, placed in the area illuminated by a passive EESS satellite with altitude h_s . We define the elevation beamforming angle α_{BF} as the angle between the direction of the beamforming steering angle and the ground. In the following, we consider geometric beamforming, i.e., the beams of the TX and of the RX are aligned to the LoS connecting the two, with an inclination $\alpha_{BF} = \alpha_{tx,rx}^{LoS}$, and θ_{HB}^{V} Half Power Beamwidth (HPBW).

For simplicity, we assume that the nodes and the satellites are aligned and consider the 2D geometry. Assuming that $h_s \gg h_{tx}, h_{rx}$, the LoS and the reflected rays emitted by the ground nodes are both amplified with gain G_S by the main lobe of the satellite sensor, due to the angular spread [36]. For this reason, in this analysis, we omit it and focus on the beamforming gain of the TX node G_{TX2S} toward the satellite.

To evaluate the interplay between the beamforming and the two rays, we consider three representative satellite nadir angles $\alpha_n = \{10^\circ, 35^\circ, 65^\circ\}$. The TX is equipped with an antenna array with a 3° HPBW and points towards the LoS to the RX. The path losses of the GR and the LoS ray are considered separately and combined destructively and constructively. The full elevation range of the beamforming angle is considered, from 0° (RX right below the TX) to 180° (RX above the TX). Fig. 4a shows how the transmitter beamforming gain G_{TX2S} amplifies the LoS (solid) and the reflected ray (dashed) as the beamforming angle changes. From Eqs. (2) and (4), the angular separation between LoS and ground reflection is $\alpha_{tx,s}^{LoS} - \alpha_i \simeq \pi - 2\alpha_s$. Thus, the only case when both rays are amplified is when $\alpha_{tx,s}^{LoS} - \alpha_i < \theta_{HB}^V \implies \frac{\pi - \theta_{HB}^V}{2} < \alpha_s$. Considering the narrow beams that will be adopted at these frequencies, this can happen only when both the satellite



(a) Beamforming gain of the terrestrial transmitter in the direction of the satellite as seen by the LoS and by the reflected ray, for different beamforming elevation angles α_{BF} .

(b) Path loss to the satellite. LoS+Refl and LoS-Refl represent the bound for constructive and destructive interference, respectively.

Fig. 4. The ground reflection to the satellite is amplified by the main lobe of the gNB pointing towards the UEs and thus to the ground.

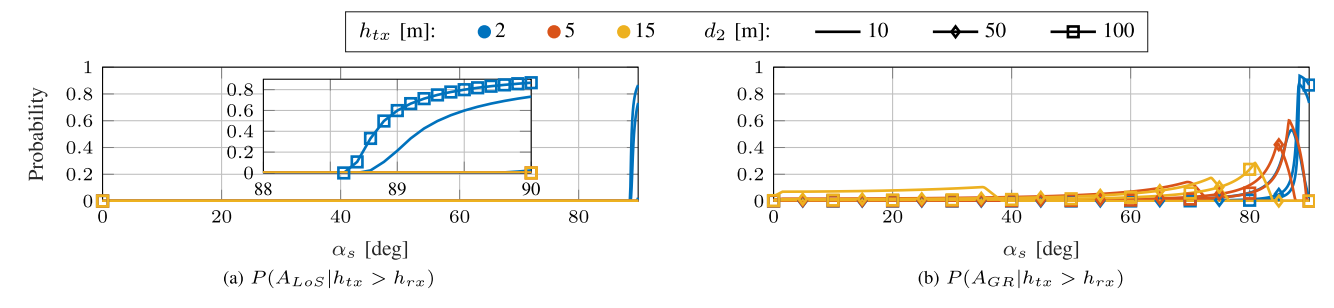


Fig. 5. Probability that the LoS $(P(A_{LoS}))$ and the reflected $(P(A_{GR}))$ rays are amplified by the main beam of the transmitting ground node.

and the beamforming direction are at the horizon. However, as mentioned in Sec. III-A, we only consider satellite angles α_s below 80° , thus excluding this case.

We can distinguish three behaviors, according to the geometric characteristics of the link:

- C1) $\alpha_{BF} < 90^{\circ} \ (h_{tx} > h_{rx})$: In this case, the TX focuses its beam towards the ground. This is generally the case for the transmission from a gNB, placed in high locations for better coverage, to a UE at the ground level. Indeed, Fig. 4a shows that the LoS ray is effectively suppressed, particularly if the satellite is well above the horizon, whereas the ground reflection is greatly amplified.
- C2) $\alpha_{BF} > 90^{\circ}$ ($h_{tx} < h_{rx}$): Conversely, in this case, the transmitter points the beam upwards, as can be the case during the communication from a UE to a gNB. Here, the ground reflection is strongly attenuated and is negligible when compared to the LoS ray.
- C3) $\alpha_{BF} \simeq 90^{\circ}$ ($h_{tx} \simeq h_{rx}$): Here, the transmitter points at the horizon, e.g., to a node at similar height or very far away. We do not consider the latter, as at sub-THz frequencies the link length is short, whereas the former can be the case in Device-to-Device (D2D) communications or backhaul links. As mentioned above, the angular separation between the two rays makes it so that in this region neither of them is amplified.

In Fig. 4b, the overall amplification of each ray is obtained by subtracting the path loss L from the corresponding transmitter gain G_{TX2S} . The role of beamforming is extremely significant, as it can greatly amplify both the interfering rays, depending on the geometry. The peak power on the left side of Fig. 4b, i.e., when the ground ray is amplified (case C2), is lower than those on the right side (case C3), and their

difference corresponds to the reflection loss. Finally, note that the superposition of the two rays is relevant only when they have similar amplitude and they have opposite phase (destructive). Specifically, when the TX beam amplifies the reflection enough to compensate for the reflection loss, the LoS and the reflected ray have comparable amplitude and cancel out. On the other hand, their constructive combination increases the aggregated power by at most 3 dB, when their phase is aligned and they have equal amplitude.

B. Probability of Beamforming Amplification

Starting from the considerations given in the previous section on the interfering power, we derive the probability of "beamforming amplification," identifying the events when the beam amplifies one of the two interfering rays, and the corresponding probabilities under some simplifying assumptions.

Let us consider only the vertical HPBW θ_{HB}^{V} of the beam generated by TX. Let $\alpha_{tx,s}^{LoS}$ be the angle between the horizontal direction at the TX and the LoS connecting the latter to the satellite. We define the event "the direct ray is amplified within the 3 dB range of the main lobe" (A_{LoS}) , with probability $P(A_{LoS})$) as $\frac{\theta_{HB}^{V}}{2} \geq |\alpha_{BF} - \alpha_{tx,s}^{LoS}|$. Similarly, for the reflected ray, the event A_{GR} (with probability $P(A_{GR})$) maps to the condition $\frac{\theta_{HB}^{V}}{2} \geq |\alpha_{BF} - \alpha_{i}|$, where α_{i} is the reflection incident angle (Eqs. (2)). Fixing the elevation angle of the satellite α_{s} , from Eqs. (2) and Eqs. (4) we have:

$$(A_{LoS}): |\alpha_{BF}| \le \left(\alpha_{tx,s}^{LoS} \pm \frac{\theta_{HB}^{V}}{2}\right) \simeq \left(\pi - \alpha_{s} \pm \frac{\theta_{HB}^{V}}{2}\right) := \theta_{LoS}^{\pm}$$

$$(13)$$

$$(A_{GR})$$
:
$$|\alpha_{BF}| \le \left(\alpha_i \pm \frac{\theta_{HB}^V}{2}\right) \simeq \left(\alpha_s \pm \frac{\theta_{HB}^V}{2}\right) := \theta_{GR}^{\pm} \qquad (14)$$

The Probability Density Function (PDF) $f_{tx,rx}^{LoS}\left(\alpha_{tx,rx}^{LoS}\right)$ of the LoS angles between the TX and the RX is fully characterized by the spatial distribution of the ground nodes. With the assumption of geometric beamforming, we can thus use the PDF of $\alpha_{tx,rx}^{LoS}$, easy to derive, in place of $f_{BF}(\alpha_{BF})$. Thus,

$$P(A_{LoS}) = \int_{\theta_{LoS}^-}^{\theta_{LoS}^+} f_{BF}(\alpha) d\alpha = \int_{\theta_{LoS}^-}^{\theta_{LoS}^+} f_{tx,rx}^{LoS}(\alpha) d\alpha$$
$$P(A_{GR}) = \int_{\theta_{GR}^-}^{\theta_{GR}^+} f_{BF}(\alpha) d\alpha = \int_{\theta_{GR}^-}^{\theta_{GR}^+} f_{tx,rx}^{LoS}(\alpha) d\alpha. \quad (15)$$

We can compute the LoS angle PDF starting from its Cumulative Distribution Function (CDF) F_{BF} , that can be derived from the distribution f_d and f_h of the TX-RX distance and of the node heights, respectively:

$$\alpha_{BF} = \arctan\left(\frac{d}{|h_{tx} - h_{rx}|}\right) := g(d, h_{tx}, h_{rx})$$

$$F_{BF}(\alpha) = \int_{D_{h_{tx}}} \int_{D_{h_{rx}}} \int_{D_{h_{d}}} f_{h_{tx}, h_{rx}, d} \left(h_{tx}, h_{rx}, d\right) dh_{tx} dh_{rx} dd$$

$$(17)$$

For simplicity, we can fix h_{tx} and limit our analysis to the case C1) identified in Sec. IV-A $(h_{tx} > h_{rx})$ and assume that the height of the RX h_{rx} and its distance d from the transmitter are statistically independent. This is representative of a downlink communication from a gNB with known height h_{tx} to the served user at unknown distance d and height h_{rx} . Then, from Eqs. (17)

$$F_{BF}(\alpha) = \int \int_{\alpha_{BF} < \alpha} f_{h_{rx},d}(h_{rx},d) \, \mathrm{d}h_{rx} \, \mathrm{d}d, \qquad (18)$$

which can be computed, if the distributions are known, by subsequently solving the two integrals using Eqs. (16) to make a change of variable or using the method of transformations.

The link length d and the node height h_{rx} can be modeled through any distribution, possibly deriving it from real data. However, for this work, without loss of generality, we assume the TX-RX 2D distance d distributed uniformly in $[d_1,d_2]$, assuming that the links are established between non-overlapping nodes $(d_1>0)$ within a maximum radius d_2 , and $h_{rx}\simeq U[h_1,h_2]$, $0< h_1< h_2< h_{tx}$. Under this assumption, we are able to derive a closed-form expression for the amplification probability and draw general conclusions:

$$F_{BF}(\alpha)$$

$$= \int_{h_1}^{h_2 \min(d_2, (h_{tx} - h_{rx}) \tan \alpha)} f_{h_{rx}, d}(h_{rx}, d) dh_{rx} dd$$

$$= \int_{h_1}^{h_2} (F_d(\min(d_2, (h_{tx} - h_{rx}) \tan \alpha)))$$
(19)

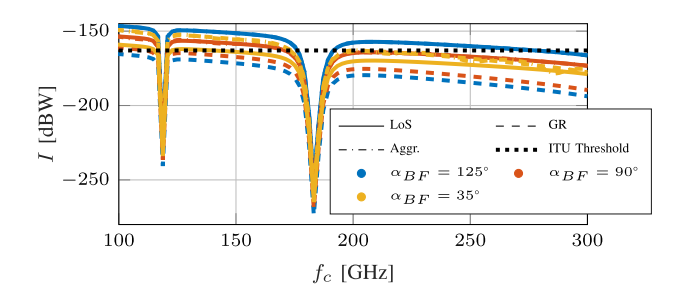


Fig. 6. Interference to the satellite for different sub-THz frequencies. The satellite is at $\alpha_n=35^\circ$ and at 400 km of altitude.

$$-F_{d}(d_{1})f_{h_{rx}}(h_{rx}) dh_{rx}$$

$$= \begin{cases} 0 & \text{if } 0^{\circ} < \alpha < \arctan\left(\frac{d_{1}}{h_{tx} - h_{rx}}\right) \\ \frac{\tan \alpha}{2\Delta d} \left(2h_{tx} - (h_{2} + h_{1})\right) \\ & \text{if } \arctan\left(\frac{d_{1}}{h_{tx} - h_{rx}}\right) < \alpha < \arctan\left(\frac{d_{2}}{h_{tx} - h_{1}}\right) \\ \frac{h_{tx} - h_{1} - d_{2}/\tan \alpha}{\Delta h} + \frac{\tan \alpha((d_{2}/\tan \alpha)^{2} - (h_{tx} - h_{2})^{2})}{2\Delta h \Delta d} \\ & \text{if } \arctan\left(\frac{d_{2}}{h_{tx} - h_{1}}\right) < \alpha < \arctan\left(\frac{d_{2}}{h_{tx} - h_{2}}\right) \\ 1 & \text{if } \arctan\left(\frac{d_{2}}{h_{tx} - h_{2}}\right) < \alpha < 90^{\circ}, \end{cases}$$

$$(21)$$

where $\Delta h = h_2 - h_1$ and $\Delta d = d_2 - d_1$.

Then, the probabilities in Eqs. (15) become, for the case under study, $P(A_{LoS}|\text{C1}) = F_{BF}(\theta_{LoS}^+) - F_{BF}(\theta_{LoS}^-)$ and $P(A_{GR}|\text{C1}) = F_{BF}(\theta_{GR}^+) - F_{BF}(\theta_{GR}^-)$. Fig. 5 reports their value for different satellite elevation angles α_s and $\theta_{HB}^V = 3^\circ$. As expected, for case C1), where $h_{tx} > h_{rx}$, the probability of amplifying the GR ray is greater than the corresponding one for LoS. Specifically, $P(A_{LoS}|\text{C1})$ is not negligible only for the edge case when the satellite is at the horizon $(\alpha_s \simeq 90^\circ)$ and the TX's height is comparable to that of the RX $(h_{tx} = 2 \text{ m})$. On the contrary, $P(A_{GR}|\text{C1})$ is significantly larger

- when the satellite is above the ground nodes ($0^{\circ} < \alpha_s \le 37.5^{\circ}$) and the TX is much higher than the RX ($h_{tx} = 15$ m), that is within 10 m;
- when the satellite is between 37.5° and 75° and the TX is much higher ($h_{tx} = 15$ m) than an RX within 10 m;
- when the satellite is at the horizon ($\alpha_s>80^\circ$). In this case, the ground reflection is less representative of practical cases, as explained in Sec. III-A.

The derivation for cases C2 and C3 is analogous.

C. Frequency

In this section, we analyze a basic example to show how the carrier frequency f_c affects the interference to the satellite. Specifically, we consider a ground node placed at height $h_{tx}=3$ m and a satellite at 400 km of altitude and $\alpha_n=35^\circ$, with antenna gains of 35 dB and 38.5 dB and HPBWs of 3° and 2° , respectively. In Fig. 6 we report the interference to the satellite for different frequencies, considering the LoS and the GR separately, as well as their superposition. For the ground node, we considered three beamforming angles, 90° (horizon,

case C3), 125° (upwards, case C2), and 35° (downwards, case C1). The power of each ray is computed by combining the path loss L derived in Eqs. (11) with the transmitter and satellite gain $G_{TX2S}(\theta_{AoD}, \phi_{AoD})$ and $G_S(\theta_{AoA}, \phi_{AoA}) = G_S$ of the TX and RX at the Angle of Departure (AoD) and Angle of Arrival (AoA), respectively:

$$I_{LoS} = P_{tx} + G_{TX2S}(\theta_{AoD}^{LoS}, \phi_{AoD}^{LoS}) + L_{LoS} + G_S$$
 (22)

$$I_{refl} = P_{tx} + G_{TX2S}(\theta_{AoD}^{refl}, \phi_{AoD}^{refl}) + L_{LoS} + G_S,$$
 (23)

$$I_{refl} = P_{tx} + G_{TX2S}(\theta_{AoD}^{refl}, \phi_{AoD}^{refl}) + L_{LoS} + G_S, \quad (23)$$

where $P_{tx} = 0$ dBW. The power of the two rays is then combined according to Eqs. (12).

First, we observe the presence of the two absorption peaks at 118 and 183 GHz, due to the presence of the oxygen molecules and of the water vapor, respectively. Secondly, we observe how the reflected ray can be amplified by the beam of the ground node, as explained in Sec. IV-A. Specifically, when the beamforming angle is 125°, the LoS ray is amplified, whereas the reflected ray is attenuated, and viceversa when the beamforming angle is 35°. Furthermore, we observe that, in the considered frequency band, the reflection loss remains almost constant, whereas the LoS path loss increases with the frequency and dictates the overall trend.

Finally, the ITU threshold [37] is exceeded particularly for frequencies below the second absorption peak. The only exception is when the ground node steers its beam toward the satellite, thus amplifying the LoS ray.

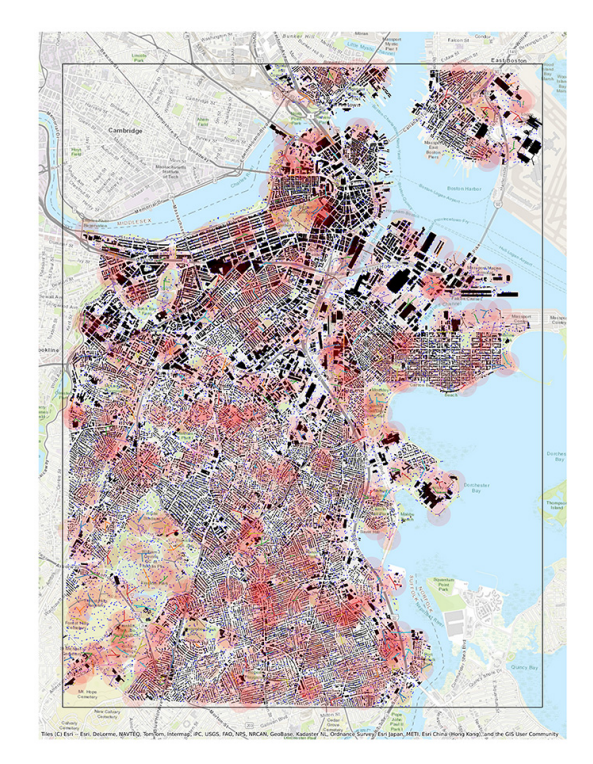
According to this observation, we selected three frequencies for the remainder of this work, 164, 178, and 240 GHz, that are representative of the three regions of the spectrum, i.e., below, close to and above the oxygen absorption peak, respectively. Accordingly, for our simulations we selected two satellites that operate in those bands, i.e., TEMPEST-D [8] for the former two and the MLS instrument on board of the Aura mission [9] for the latter.

V. SIMULATION SETUP

In this and the following section, we report the setup and results of an extensive analysis of the RFI in different scenarios. The mathematical analysis in Sec. IV-B allowed us to gain a deep understanding of the simulation results, identifying the most significant elements that contribute to the overall power that reaches an incumbent satellite. Through simulations, we are able to drop the simplifying and ideal assumptions that were required in the analytical derivation, and accurately quantify the RFI in realistic and complex scenarios. Finally, in this section we provide useful insights and guidelines for the study and simulation of the RFI at sub-THz frequencies, that will help the study and design of coexistence solutions.

A. Scenarios

For this analysis, we consider two representative outdoor scenarios, the *Urban Cellular* and the *Backhaul* scenarios, both set in the city of Boston, MA, USA. The two present inherently different characteristics, e.g., different types of nodes and beamforming angle distributions, thus producing different interference patterns.



Map of Boston with interfering nodes ($\lambda_g = 10$). The red areas represent the coverage of each gNB ($d_{MAX} = 200 \text{ m}$ in the Urban scenario).

TABLE I NETWORK PARAMETERS FOR THE SIMULATION CAMPAIGN

	gNB (Urban/Backhaul)	UE (Urban)
P_{TX} [dBm]	10/30	10
G_{MAX} [dB]	35	24.5
θ_{HB} [deg]	3	10
N^{SEC}	3	1
Height [m]	$\{3, 5, 8, 10, 15\}$	$\mathcal{U}([1.6, 1.8])$

TABLE II SPECIFICATIONS OF THE CONSIDERED SATELLITES

	TEMPEST [8]	Aura MLS [9]
θ_{HB} [deg] f_c [GHz] Altitude [km] Scan Mode I_{th} [dBW] [37]	1.68/1.72 164/178 400 Conical –163	0.066 [38] 240 705 Limb -194

1) Map: We use data from the city of Boston to (i) select realistic locations for the terrestrial nodes and to (ii) characterize the path obstruction from the terrestrial network to the satellite. To do that, we extract terrain data and the road network from OSM using OSMnx [39] to reject the nodes spawned in invalid locations (e.g., on water surfaces) and to move indoor nodes outside the building footprint, respectively, as explained in the following paragraphs. To analyze the obstruction of the paths from the terrestrial network to the satellite, we used the 3D model of the buildings published by the Boston Planning & Development Agency.¹

¹ www.bostonplans.org/3d-data-maps/3d-smart-model/3d-data-download

- 2) Node Characteristics: We define two types of nodes: the gNBs and the UEs (see Table I). The former represents a generic fixed node that can transmit using a large antenna array and thus a narrow beam ($\theta_{HB}=3^{\circ}$). Each gNB has $N_{gNB}^{SEC}=3~120^{\circ}$ -wide angular sectors, according to the current 3rd Generation Partnership Project (3GPP) guidelines. The UEs represent mobile nodes with more limited beamforming capabilities ($\theta_{HB}=10^{\circ}$). A single sector is available to the UE. For both gNBs and UE, in each sector a single link at a time can be active.
- 3) Node Placement: First, N_{qNB} tentative gNB locations are generated on the map according to a Poisson Point Process (PPP) with a given density λ_q . Then, the nodes are placed according to an iterative procedure loosely based on a Rejection Sampling process: the gNBs that overlap with the building footprint (i.e., indoor) or that are in invalid areas (e.g., water bodies) are projected to the nearest street using OSMnx [39]. The points for which this is not possible (e.g., the nearest street is an underground road, or two points overlap) are rejected, an equal number of new points are generated, and the procedure is iterated until all the nodes are successfully moved outside. Finally, for the Urban Cellular scenario, N_{UE} UEs are placed on the map with the same iterative procedure. According to [40], we deterministically set $N_{UE} = N_{gNB} \times N_{gNB}^{SEC} \times 10$. Thus, the number of nodes for each scenario is fully characterized by λ_g .

Three gNB densities were considered, $\lambda_g \in \{10,45,100\}$ gNBs/km². In addition, we consider the number and location of gNBs that were approved by the City of Boston² as a fourth scenario named *Real*, with $\lambda_g \simeq 18$ gNBs/km².

4) Attachment: In the Urban Cellular scenario, the UEs are assigned to gNBs according to the following algorithm: first, each UE is tentatively assigned to the closest gNB. If the distance d between the UE and the nearest gNB is larger than $d_{max}=200$ m, the UE can not be served by any gNB and remains unattached, and the process is terminated. Otherwise, if the LoS between the UE and the gNB is unobstructed by the buildings, the assignment is confirmed and the process is terminated. If, on the contrary, the LoS is obstructed, the UE is assigned to the second-closest gNB, and the procedure is repeated from the distance-check step. Each UE in coverage is thus assigned a single gNB, and each sector of the gNB is assigned a list of UEs that it can serve.

In the Backhaul scenario, links are established between gNBs. First, a list with all the gNB pairs that are in LoS is computed. Then, for each link, a random direction for the data flow is picked. For each sector of the gNBs, a single link can be active at any given time.

5) Beamforming: The beam of each node is simulated using the ITU antenna pattern shown in Fig. 4a. The choice is justified both by the ITU recommendations and by computational efficiency, as computing the beamforming vectors and gains for the large areas and the corresponding number of nodes considered in this analysis is extremely

²The data is available in the Boston Open Data archive at https://tinyurl.com/2xjn9m43

demanding from a computational point of view. In both scenarios, geometric beamforming is considered, i.e., the beams of the TX and of the RX are aligned to the LoS direction connecting the two.

B. Satellite Model

Earth-exploration satellites can be classified as conical-(C), nadir- (N) or limb-viewing (L) [37], depending on the geometry of their scan mode. The nadir scan mode views the Earth's surface at angles of nearly perpendicular incidence. The scan can terminate on the ground or at various levels in the atmosphere. The conical scan points its radiation pattern to the Earth's surface by rotating the antenna at an offset angle from the nadir direction, projecting its footprint to the ground. The limb scan mode looks at the edge of the atmosphere and terminates in space rather than on the surface. In this work, we consider conical and limb satellites, as they have different behavior when considering RFI from terrestrial systems. The conical and the nadir-viewing satellites might amplify the interference from a ground network by pointing directly at it, whereas the limb-viewing attenuates the signals coming from the Earth's surface. Note that for this analysis, the nadir scan mode can be seen as a particular case of the conical scan, when the latter points at the Earth's surface with an inclination angle close to nadir. We model them using the specifications of the TEMPEST-D satellites [8] and of the MLS on the Aura mission [9], and consider a bandwidth representative of the specifications of such sensors [41]. The most relevant characteristics for this study are reported in Table II.

For a given nadir angle α_n , the location of the satellite is determined by considering a conical scan geometry and assuming that the main lobe of the satellite points at the center of the considered area. That is, we fix α_n and thus determine the horizontal x and the vertical distance h_{sat} from the center of the ground network, according to the geometry and notation shown in Fig. 1. Given the importance of the geometry and of the obstruction by the buildings, we consider three representative nadir angles α_n , as in Secs. IV, and sample the azimuth space α_{az} with a sampling step of 10° for both satellites.

The same angular positions (α_n, α_{az}) are then also used for the limb satellite, steering the main beam so that it points at the atmosphere. That is, the MLS radiation pattern points 10 km above the ground network, while the TEMPEST one illuminates it, according to the respective scan mode.

VI. NUMERICAL RESULTS

In this section, we present the results obtained through numerical simulations employing the setup presented in Secs. V. Specifically, in Sec. VI-A we report the results for the Urban Cellular scenario, evaluating the effect of the obstruction on the number of interfering nodes, the distribution of their gain, the aggregated power, the impact of different carrier frequencies and of different network load factors. Similarly, in Sec. VI-B we report the beamforming gain of the ground nodes toward the satellite and the aggregated interference of the backhaul network.

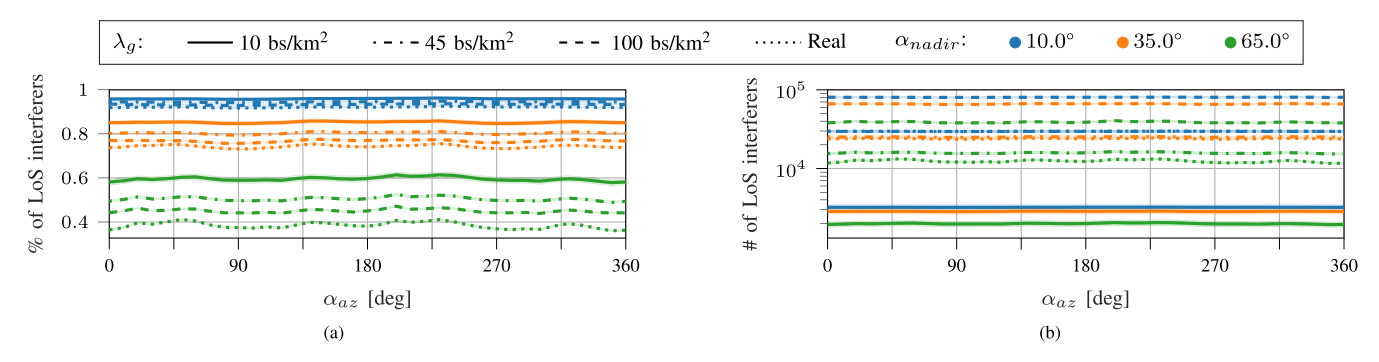


Fig. 8. Percentage (a) and number (b) of nodes not obstructed by the buildings for different satellite nadir angles and gNB densities, varying the satellite azimuth location.

A. Urban Cellular

a) Number of interfering nodes: The first step in estimating the aggregated power is to determine which paths reach the satellite without being obstructed by buildings. We assume that whenever a ray impinges on a building, it is absorbed or diffusely scattered and not reflected. We identify such rays with a geometric obstruction check, commonly used in ray tracers, optimized considering the characteristics of the ground-to-satellite path, e.g., only buildings within a certain radius and tall enough can block the paths to the satellite. Accordingly, we define as a potential interferer any ground node whose LoS ray with the satellite is unobstructed by buildings. Finally, to reduce the computational complexity, we assume that if the LoS ray is obstructed by a building, so is the ground-reflection one, without loss of generality. The percentage and the number of potential interferers are reported in Fig. 8a and Fig. 8b, respectively. The x axis reports the azimuth of the satellite. Although the obstruction by the buildings plays a fundamental role, we can observe that the azimuth position of the satellite α_{az} does not significantly affect the considered metrics, as the fluctuations are limited. This suggests that the building distribution is homogeneous in the azimuth domain, with some variations visible when considering large angles ($\alpha_n \simeq 65^\circ$). Considering the percentage of (un)obstructed nodes allows us to draw conclusions that are independent of the absolute number of nodes. Fig. 8a shows that the percentage of ground nodes that can interfere with the satellite is strongly correlated to the nadir angle: when the satellite is above the city ($\alpha_n \simeq 10^\circ$), the interfering signal propagates in the vertical direction, limiting the number of buildings that block it. Thus, almost 100% ground nodes are in LoS with the satellite. As the satellite moves towards the horizon, the percentage decreases, with almost 80% of the ground nodes able to reach it when it is at $\alpha_n = 35^{\circ}$, and as little as 50% when it is at $\alpha_n = 65^{\circ}$.

On the contrary, the absolute number of potential interferers reported in Fig. 8b is grouped by gNB density, as expected. However, the effect of the α_n angle is still clearly visible, as for each density the number of potential interferers decreases as the satellite approaches the horizon.

b) Interfering nodes gain: As shown in Sec. IV-B, although the TX focuses the emitted power toward the RX through narrow beams, there is a non-zero probability that

also the interfering rays to the satellite are amplified by the beamforming configuration of the TX. Fig. 9 reports the estimated PDF of the transmitter gain experienced by the interfering LoS and reflected rays that reach the satellite. For all the nadir angles, the vast majority of the rays are successfully suppressed $(G_{TX2S} < 0)$.

In particular, the UEs suppress the RFI with the minimum gain with high probability, corresponding to the peak probability in -8.5 dBi, that is clearly visible for $\alpha_n = 35^{\circ}$ and $\alpha_n = 65^{\circ}$. On the contrary, the same behavior is not present when considering the gNBs, where a broader interval of G_{TX2S} has a high probability. This is due to the fact that the interference, and hence the gain reported in Fig. 9, is computed only for the rays emitted by the angular sector containing the satellite. Given that the UEs have a single sector, all the rays are included for the PDF estimation, even when the antenna is pointing in the opposite direction. On the contrary, only the transmitter gain of the rays in the gNB sector containing the satellite is considered, based on the realistic assumption that the power leakage by a sector to the adjacent ones can be effectively suppressed. Thus, the gNB gains reported in Fig. 9 are computed only in the 120° angular sector containing the satellite instead of the whole 360° azimuth domain, thus increasing the probability of the antenna pointing toward the satellite in the azimuth plane.

Furthermore, Fig. 9 shows a distinct distribution for the LoS and for the ground-reflected rays when considering the gNBs and the UEs. Specifically, the LoS rays of the UEs have a greater probability of being amplified than the GR rays, and vice-versa for the gNBs. The zoom on the tails of the PDF highlights this behavior, with the highest gain being experienced by the GR (LoS) rays of the gNBs (UEs). This trend can be traced back to the analysis presented in Sec. IV-B: the UEs point upwards to the gNBs (case C2), amplifying the GR more than the LoS. Conversely, the gNBs point to the UEs and thus toward the ground, increasing the probability of amplifying the GR.

Moreover, all the estimated PDFs have multiple peaks, typical of the multimodal distributions. Again, referring to the analysis of Sec. IV-B, we can trace this behavior back to the discrete distribution of the gNB heights in relation to the beam characteristics and the satellite positions. This favors some beamforming angles, and thus some G_{TX2S} .

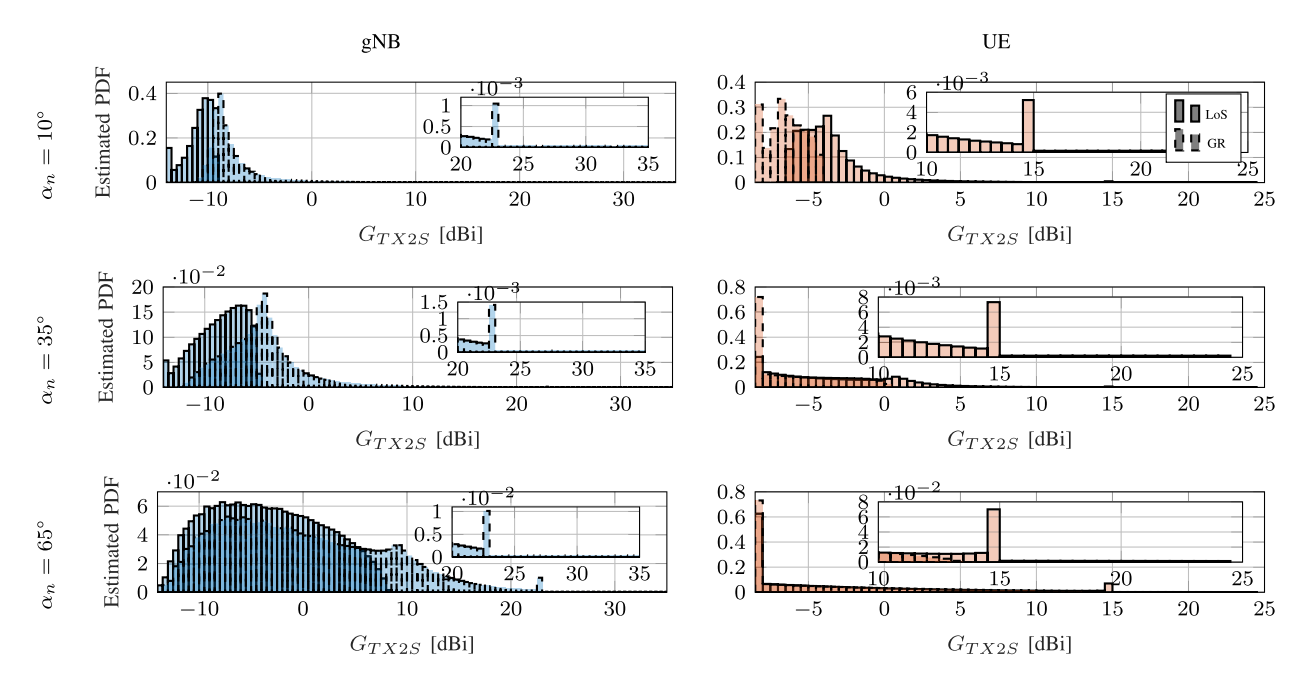


Fig. 9. Estimated PDF of the G_{TX2S} of the interfering rays for different satellite nadir angles in the Urban scenario.

Finally, also in this analysis, the elevation of the satellite plays a fundamental role. Firstly, we can observe the dramatic change in the shape of the distributions in the six plots of Fig. 9. For $\alpha_n = 10^{\circ}$, both the LoS and the GR rays are strongly suppressed. Looking at Fig. 4a, this can be explained by the fact that the maximum amplification with this satellite elevation is obtained with extreme beamforming angles ($\alpha_{BF} \simeq 10^{\circ}$ or $\alpha_{BF} \simeq 172^{\circ}$), which are not common. On the contrary, when the satellite is at a lower elevation angle, the interfering LoS and GR rays are more often aligned with the beams, resulting in a more uniform distribution of the transmitter gain. However, a satellite at lower elevation angles also implies that ground-to-satellite signals need to traverse a longer portion of the atmosphere, as we discuss next, and have a higher blockage probability, as discussed above.

c) Aggregated power: Fig. 10 reports the Empirical Cumulative Distribution Functions (ECDFs) of the aggregated RFI power at the satellite for different nadir angles and for different gNB densities. For each Monte Carlo iteration, the total RFI is obtained by combining the electric fields at the receiver according to Eqs. (12), thus accounting also for the phase difference. In particular, to analyze the different contributions to the overall power, we sum all the interfering power generated by the LoS (solid) and by the reflected (dashed) rays, aggregating the gNBs (blue) and of the UEs (orange). The LoS and reflected rays of the individual ground nodes are then combined according to Eqs. (12) (dash-dotted). Similarly, the overall RFI power (yellow) is obtained by combining all the aforementioned contributions. In each Monte Carlo iteration, we assume that all the gNB sectors either transmitting or receiving (with probability $P_{TX} = P_{RX} =$ 0.5) to a randomly selected UE among the one assigned to it. The sectors without assigned users remain silent.

First, we can observe that the power delivered by the LoS rays of the UEs to the satellite dominates the other contributions in almost all of the considered cases. This is due (i) to the fact that we consider a single gNB sector, as previously explained, as we assume that the gNBs can effectively suppress the inter-sector leakage. The same assumption does not hold for the UEs, due to the constantly-changing orientation of the hand-held devices. Furthermore, (ii) the UEs' beam amplifies their LoS ray to the satellite. On the contrary, the GR ray of the UEs is effectively suppressed. Conversely, the reflection from the gNBs to the satellite is stronger than the corresponding direct ray in almost all scenarios.

Secondly, as the satellite approaches the horizon, the overall RFI decreases. This is due to (i) the lower number of interfering nodes due to the obstruction by the buildings, as illustrated at the beginning of this section, and to (ii) the greater path loss due to the larger distance of the satellite from the ground network. Furthermore, we observe that for higher nadir angles, the impact of the reflections is also increased, taking over that of the direct rays. Again, this is due to the considerations on the transmitter gain given in the previous paragraph.

Thirdly, we notice that, as expected, the overall RFI increases with the number of nodes. For reference, Fig. 8b reports the potential number of interferers for each density and nadir angle, although not all the nodes are simultaneously active. In Fig. 10, we report also the average interference generated by a single ground node (dotted). Note that the gap between the ECDF and the corresponding average interference is due to the aggregation of the RFI over the network. Considering the number in Fig. 8b, one might expect a larger difference, as we aggregate the power of several thousands of ground nodes, that would correspond to tens of dBs if we just

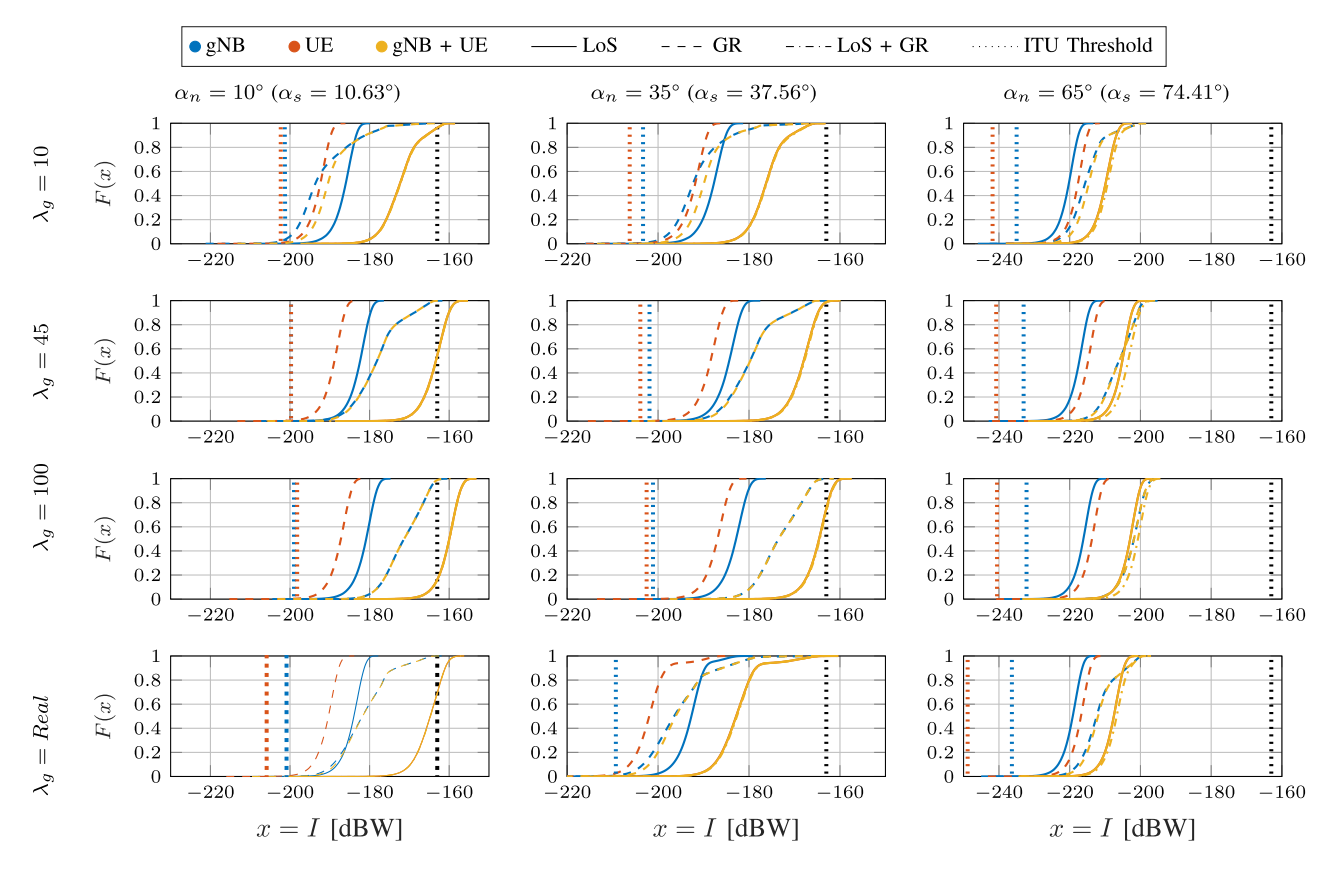


Fig. 10. ECDF of the RFI power at the incumbent satellite, for different nadir angles and different gNB densities. For these results, we consider the TEMPEST satellite at 178 GHz.

TABLE III PROBABILITY THAT THE RFI IS GREATER THAN THE ITU THRESHOLD FOR THE CELLULAR SCENARIO, FOR THE TEMPEST SATELLITE AT 178 GHz. For $\alpha_n=65$ degrees, the Probability Is Always 0

		α_n [deg]		α_n [deg]			α_n [deg]			
⊒7		10	35		10	35			10	35
s/k	10	0/0.0371/0.0368	0/0/0	10	0/0/0	0/0/0	_	10	0.0368	0
æ	45	0/0.4537/0.4537	0/0.012/0.012	45	8e - 4/0/7e - 4	1.5e - 4/0/1e - 5		45	0.4548	0.0148
<u></u>	100	0/0.8385/0.8385	0/0.2473/0.2469	100	0.0124/0/0.0124	0.0011/0/7.5e - 4		100	0.8415	0.27
8	Real	0/0.3102/0.3102	0/1.85e - 4/1.71e - 4	Real	1.3e - 4/0/1.15e - 4	0/0/0		Real	0.3120	3.3e - 4
		(a) LoS (gNB/UE/com	bined)		(b) Ground Reflection (gNB/	UE/combined)			(c) Aggrega	ated

summed the electrical field intensities at the satellite. However, due to the phase difference among the received signals, the overall interference is reduced, as a large percentage of signals superimpose destructively, canceling out.

Finally, Table III reports the probability that the total aggregated RFI at the satellite is greater than the ITU threshold for the acceptable RFI at the considered frequency ($I_{th}=-163~{\rm dBW}$ [37]). The greatest interference is observed when the satellite is orbiting over the terrestrial network ($\alpha_n=10^\circ$) and with $\lambda_g=100~{\rm gNBs/km^2}$. For the same satellite position, even as little as $\lambda_g=10~{\rm gNBs/km^2}$ is enough to cause significant interference to the satellite. On the contrary, when the satellite is at the horizon, the RFI is well below the safety levels.

d) Frequency: The results presented so far in this section were obtained considering $f_c = 178$ GHz, where the propagation is characterized by a strong absorption by the atmospheric gases. Here, we compare the RFI observed by TEMPEST at 164 GHz, which is characterized by a lower

absorption, at 178 GHz, and at 240 GHz, that is used by Aura. The results for the latter are analyzed in depth in the next paragraph. Fig. 11 reports the aggregated RFI for the three frequencies. Specifically, at 240 GHz it is well below the ITU threshold (–194 dBW for limb scanners), even when considering a high gNB density ($\lambda_g=100~{\rm gNBs/km^2}$) and $\alpha_n=10^{\circ}$. Conversely, for 164 GHz, even when the RFI is the weakest ($\alpha_n=65^{\circ}$ and $\lambda_g=10~{\rm gNBs/km^2}$), it is above the threshold with a probability of 0.09. We can thus conclude that transmitting at frequencies close to the absorption peaks can indeed help mitigate the RFI, whereas transmitting in lower-absorption bands can almost certainly cause significant interference to conical-scan satellites.

e) MLS: As reported in Fig. 6, the RFI at the satellite antenna at 240 GHz can be higher than at 178 GHz. The large difference in interfering power observed in Fig. 11 is due to the different altitudes (705 km Aura vs 400 km TEMPEST) and scan modes of the satellites. While the TEMPEST satellite has a conical scanning sensor, the Aura

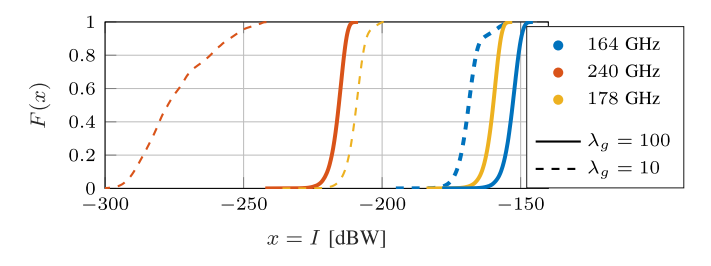


Fig. 11. Aggregated RFI observed by TEMPEST at 164 GHz and 178 GHz and by Aura at 240 GHz.

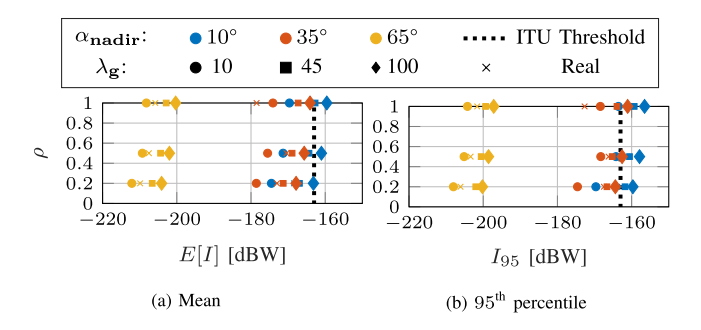


Fig. 12. Aggregated interference with different network load factors.

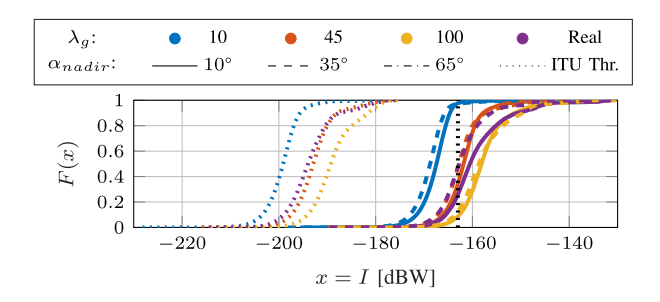


Fig. 13. Distribution of the aggregated RFI in the Backhaul scenarios.

satellite observes the limb layers of the atmosphere. Thus, the beam of TEMPEST amplifies the interference coming from the ground with maximum gain, whereas the MLS strongly attenuates it.

f) Network load factor: In Fig. 12 we show the total RFI for different network load factors. We define the network load factor through the activation probability ρ , which determines whether a gNB sector is active, i.e., on average a fraction ρ of the possible communication links is active. For instance, the aggregated interference reported in Fig. 10 assumes that all the gNB sectors are active (either transmitting or receiving), corresponding to $\rho = 1$. Fig. 12 shows the mean and the 95th percentile of the aggregated RFI for $\rho \in$ $\{0.2, 0.5, 1\}$. A load factor of 0.2 or 0.5 effectively decreases the average interference E[I] below the ITU threshold for all the considered scenarios. Conversely, the 95th percentile I_{95} is less affected, remaining above the threshold when considering high density ($\lambda_q = 45,100 \text{ gNBs/km}^2$) and small nadir angles ($\alpha_n=10^\circ$). Note that sub-THz networks with ultra-wide bandwidths are more likely to operate in scenarios with a small ρ , as transmissions can leverage high data rates and thus occupy the channel for reduced periods of time [1].

TABLE IV
PROBABILITY THAT THE RFI IS GREATER THAN THE
ITU THRESHOLD FOR THE BACKHAUL SCENARIO

	α_n [deg]					
	10	35	65			
10	0.023	0.028	0			
45	0.655	0.527	0			
Real	0.74	0.527	0			
100	0.9138	0.872	0			

B. Backhaul

a) Interfering Nodes Gain: For the backhaul scenario, links are established between gNBs, i.e., between nodes at similar heights. Thus, the transmitting beams are generally more aligned to the horizontal axis than those of their cellular counterpart. This behavior can be clearly observed in Fig. 14, where the histogram for the transmitter gain is reported, considering the TEMPEST satellite. We can observe how, due to the horizontal orientation, the beamforming effectively suppresses the interference, particularly when the satellite is above the network area ($\alpha_{BF} \in \{10^\circ, 35^\circ\}$). As it lowers toward the horizon, larger gains become more probable. Furthermore, for the same reason, the gain of the LoS and reflected rays present almost the same distribution.

b) Aggregated power: Fig. 13 reports the ECDF of the aggregated RFI in the considered scenarios, for the TEMPEST satellite at 178 GHz. We can observe that the aggregated power here is much greater than in the cellular scenario. This is mainly due to the increase in the transmitting power, which shifts all the distributions by about 20 dB.

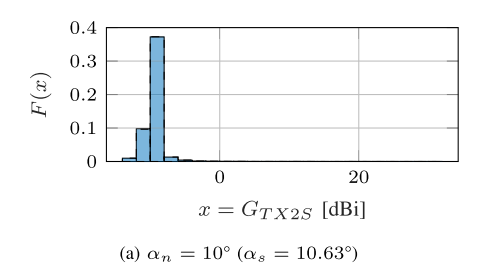
The probability of exceeding the threshold in the different scenarios is reported in Table IV. Comparing it with the results reported in Table III, we can observe how the backhaul scenario generates much greater interference than the Urban Cellular one.

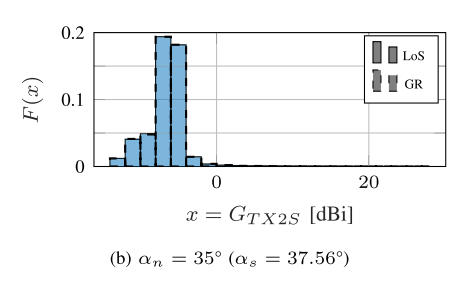
In conclusion, although the narrow beams suppress the power leaking toward the satellite, a backhaul network with the considered frequency can be potentially harmful to the incumbent satellites.

VII. CONCLUSION AND FUTURE WORKS

In this paper, we introduced analytical and simulation methodologies for the evaluation of RFI that next-generation terrestrial networks may introduce in passive sensing satellite systems. We developed a single-link analysis that shows the effect of beam amplification through the combined effect of the problem geometry, of the beam of the terrestrial TX and of the satellite. We then extended this into a large-scale data-driven simulation which relies on topologies for networks and buildings based on real-world data. The results show that—despite the high propagation and absorption loss at sub-THz frequencies—it is possible to generate RFI above ITU thresholds with specific network and satellite configurations.

These insights provide a foundation for our future work, which will focus on developing coexistence methods in a realistic data-driven framework. In addition, we will further





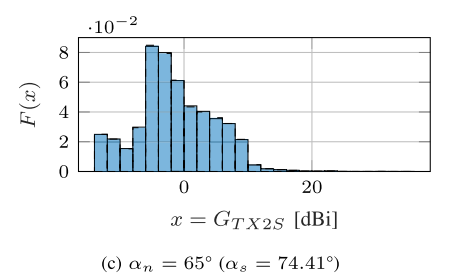


Fig. 14. Estimated PDF of the G_{TX2S} of the interfering rays for different satellite nadir angles in the Backhaul scenario.

extend our analysis by considering models for how RFI propagates into the passive sensors measurements.

REFERENCES

- I. F. Akyildiz, C. Han, Z. Hu, S. Nie, and J. M. Jornet, "Terahertz band communication: An old problem revisited and research directions for the next decade," *IEEE Trans. Commun.*, vol. 70, no. 6, pp. 4250–4285, Jun. 2022.
- [2] Attenuation By Atmospheric Gases and Related Effects, document Rec. ITU-R P.676-13, ITU, 2022.
- [3] V. Petrov, T. Kurner, and I. Hosako, "IEEE 802.15.3d: First standardization efforts for sub-Terahertz band communications toward 6G," *IEEE Commun. Mag.*, vol. 58, no. 11, pp. 28–33, Nov. 2020.
- [4] M. Polese et al., "Coexistence and spectrum sharing above 100 GHz," Proc. IEEE, vol. 111, no. 8, pp. 928–954, Aug. 2023.
- [5] C. D. Kummerow et al., "Hyperspectral microwave sensors— Advantages and limitations," *IEEE J. Sel. Topics Appl. Earth Observ. Remote Sens.*, vol. 15, pp. 764–775, 2022.
- [6] M. Polese et al., "Dynamic spectrum sharing between active and passive users above 100 GHz," *Commun. Eng.*, vol. 1, no. 1, p. 6, May 2022.
- [7] Y. Xing and T. S. Rappaport, "Terahertz wireless communications: Cosharing for terrestrial and satellite systems above 100 GHz," *IEEE Commun. Lett.*, vol. 25, no. 10, pp. 3156–3160, Oct. 2021.
- [8] S. C. Reising et al., "Overview of temporal experiment for storms and tropical systems (TEMPEST) CubeSat constellation mission," in *IEEE MTT-S Int. Microw. Symp. Dig.*, May 2015, pp. 1–4.
- [9] J. W. Waters et al., "The earth observing system microwave limb sounder (EOS MLS) on the Aura satellite," *IEEE Trans. Geosci. Remote Sens.*, vol. 44, no. 5, pp. 1075–1092, May 2006.
- [10] J. Park, E. Lee, S.-H. Park, S.-S. Raymond, S. Pyo, and H.-S. Jo, "Modeling and analysis on radio interference of OFDM waveforms for coexistence study," *IEEE Access*, vol. 7, pp. 35132–35147, 2019.
- [11] M. J. Marcus, "Harmful interference and its role in spectrum policy," Proc. IEEE, vol. 102, no. 3, pp. 265–269, Mar. 2014.
- [12] C. Bosso, P. Sen, X. Cantos-Roman, C. Parisi, N. Thawdar, and J. M. Jornet, "Ultrabroadband spread spectrum techniques for secure dynamic spectrum sharing above 100 GHz between active and passive users," in *Proc. IEEE Int. Symp. Dyn. Spectr. Access Netw. (DySPAN)*, Dec. 2021, pp. 45–52.
- [13] F. Guidolin, M. Nekovee, L. Badia, and M. Zorzi, "A study on the coexistence of fixed satellite service and cellular networks in a mmWave scenario," in *Proc. IEEE Int. Conf. Commun. (ICC)*, Jun. 2015, pp. 2444–2449.
- [14] C. Su, X. Han, X. Yan, Q. Zhang, and Z. Feng, "Coexistence analysis between IMT-advanced system and fixed satellite service system," in *Proc. IEEE Mil. Commun. Conf.*, Oct. 2014, pp. 1692–1697.
- [15] A. J. Gasiewski, C. S. Ruf, M. Younis, and W. Wesbeck, "Impacts of mobile radar and telecommunications systems on Earth remote sensing in the 22–27 GHz range," in *Proc. IEEE Int. Geosci. Remote Sens.* Symp., vol. 3, Jun. 2002, pp. 1679–1681.
- [16] W. A. Hassan, H.-S. Jo, and A. R. Tharek, "The feasibility of coexistence between 5G and existing services in the IMT-2020 candidate bands in Malaysia," *IEEE Access*, vol. 5, pp. 14867–14888, 2020.
- [17] G. Hattab, P. Moorut, E. Visotsky, M. Cudak, and A. Ghosh, "Interference analysis of the coexistence of 5G cellular networks with satellite Earth stations in 3.7–4.2 GHz," in *Proc. IEEE Int. Conf. Commun. Workshops (ICC Workshops)*, May 2018, pp. 1–6.

- [18] A. Alkhateeb, O. El Ayach, G. Leus, and R. W. Heath, "Hybrid precoding for millimeter wave cellular systems with partial channel knowledge," in *Proc. Inf. Theory Appl. Workshop (ITA)*, Feb. 2013, pp. 1–5.
- [19] L. Zhong, D. Zhou, R. Liu, X. Wang, and X. Meng, "The feasibility of coexistence between IMT-2020 and inter-satellite service in 26 GHz band," in *Proc. Int. Wireless Commun. Mobile Comput. (IWCMC)*, Jun. 2020, pp. 1006–1011.
- [20] S. P. Winter and A. Knopp, "Statistics of terrestrial fixed service interference in the aeronautical SATCOM channel," in *Proc. IEEE Int. Conf. Commun. (ICC)*, May 2019, pp. 1–7.
- [21] Y. Cho, H. Kim, E. E. Ahiagbe, and H.-S. Jo, "Spectral coexistence of IMT-2020 with fixed-satellite service in the 27–27.5 GHz band," in *Proc. Int. Conf. Inf. Commun. Technol. Converg. (ICTC)*, Oct. 2018, pp. 1–6.
- [22] Y. Cho, H. Kim, D. K. Tettey, K.-J. Lee, and H.-S. Jo, "Modeling method for interference analysis between IMT-2020 and satellite in the mmWave band," in *Proc. IEEE Globecom Workshops (GC Wkshps)*, Dec. 2019, pp. 1–6.
- [23] Y. Cho, H.-K. Kim, M. Nekovee, and H.-S. Jo, "Coexistence of 5G with satellite services in the millimeter-wave band," *IEEE Access*, vol. 8, pp. 163618–163636, 2020.
- [24] R. Aghazadeh Ayoubi et al., "IMT to satellite stochastic interference modeling and coexistence analysis of upper 6 GHz-band service," *IEEE Open J. Commun. Soc.*, vol. 4, pp. 1156–1169, 2023.
- [25] W. C. Jakes and D. C. Cox, Microwave Mobile Communications. Hoboken, NJ, USA: Wiley, 1994.
- [26] C. Han, A. O. Bicen, and I. F. Akyildiz, "Multi-ray channel modeling and wideband characterization for wireless communications in the terahertz band," *IEEE Trans. Wireless Commun.*, vol. 14, no. 5, pp. 2402–2412, May 2015.
- [27] D. Kotz, C. Newport, R. S. Gray, J. Liu, Y. Yuan, and C. Elliott, "Experimental evaluation of wireless simulation assumptions," in *Proc.* 7th ACM Int. Symp. Modeling, Anal. Simulation Wireless Mobile Syst., Oct. 2004, pp. 78–82.
- [28] F. Fund, R. Lin, T. Korakis, and S. S. Panwar, "How bad is the flat Earth assumption? Effect of topography on wireless systems," in *Proc. 14th Int. Symp. Modeling Optim. Mobile, Ad Hoc, Wireless Netw. (WiOpt)*, May 2016, pp. 1–5.
- [29] S. Loyka and A. Kouki, "Using two ray multipath model for microwave link budget analysis," *IEEE Antennas Propag. Mag.*, vol. 43, no. 5, pp. 31–36, Oct. 2001.
- [30] M. J. Feuerstein, K. L. Blackard, T. S. Rappaport, S. Y. Seidel, and H. H. Xia, "Path loss, delay spread, and outage models as functions of antenna height for microcellular system design," *IEEE Trans. Veh. Technol.*, vol. 43, no. 3, pp. 487–498, Aug. 1994.
- [31] M. Dottling, A. Jahn, D. Didascalou, and W. Wiesbeck, "Two- and three-dimensional ray tracing applied to the land mobile satellite (LMS) propagation channel," *IEEE Antennas Propag. Mag.*, vol. 43, no. 6, pp. 27–37, Dec. 2001.
- [32] T. Soler and D. W. Eisemann, "Determination of look angles to geostationary communication satellites," *J. Surveying Eng.*, vol. 120, no. 3, pp. 115–127, Aug. 1994.
- [33] R. Piesiewicz, C. Jansen, D. Mittleman, T. Kleine-Ostmann, M. Koch, and T. Kurner, "Scattering analysis for the modeling of THz communication systems," *IEEE Trans. Antennas Propag.*, vol. 55, no. 11, pp. 3002–3009, Nov. 2007.
- [34] Effects of Building Materials and Structures on Radiowave Propagation Above About 100 MHz, document Rec. ITU-R P.2040-2, ITU, 2040.
- [35] K. Du, O. Ozdemir, F. Erden, and I. Guvenc, "Sub-terahertz and mmWave penetration loss measurements for indoor environments," in *Proc. IEEE Int. Conf. Commun. Workshops (ICC Workshops)*, Jun. 2021, pp. 1–6.

- [36] F. Saggese, F. Chiariotti, K. Kansanen, and P. Popovski, "Efficient URLLC with a reconfigurable intelligent surface and imperfect device tracking," 2022, arXiv:2211.09171.
- [37] Performance and Interference Criteria for Satellite Passive Remote Sensing, document Rec. ITU-R RS.2017-0, ITU, 2017.
- [38] R. E. Cofield and P. C. Stek, "Design and field-of-view calibration of 114–660-GHz optics of the Earth observing system microwave limb sounder," *IEEE Trans. Geosci. Remote Sens.*, vol. 44, no. 5, pp. 1166–1181, May 2006.
- [39] G. Boeing, "OSMnx: New methods for acquiring, constructing, analyzing, and visualizing complex street networks," *Comput., Environ. Urban Syst.*, vol. 65, pp. 126–139, Sep. 2017.
- [40] Study on Scenarios and Requirements for Next Generation Access Technologies, Standard TR 38.913, V14.1.0, 3GPP, 2017.
- [41] W. Berg et al., "Calibration and validation of the TEMPEST-D CubeSat radiometer," *IEEE Trans. Geosci. Remote Sens.*, vol. 59, no. 6, pp. 4904–4914, Jun. 2021.



Paolo Testolina (Member, IEEE) received the B.Sc. degree in information engineering, the M.Sc. degree in telecommunication engineering, and the Ph.D. degree in information engineering from the University of Padova, in 2016, 2018, and 2023, respectively. During the master's study, he visited Universitat Politecnica de Catalunya, where he completed the master's thesis with the Remote Sensing Laboratory (RSLAB). During the Ph.D. study, he has collaborated with NIST and Toyota North America. He visited the Institute for the

Wireless Internet of Things (WIoT), Northeastern University, where he is currently a Post-Doctoral Research Fellow. His research focuses mainly on wireless networks, from channel modeling to link layer simulation, traffic modeling, spectrum sharing, interference modeling, and vehicular networks. He received the First Prize at the IEEE R8–GITEX AI Doctorate Symposium in 2023.



Michele Polese (Member, IEEE) received the Ph.D. degree from the Department of Information Engineering, University of Padova, in 2020. Then, he joined Northeastern University, Boston, as a Research Scientist and a part-time Lecturer in 2020, where he has been a Research Assistant Professor with the Institute for the Wireless Internet of Things, since October 2023. During the Ph.D. study, he visited New York University (NYU); AT&T Labs, Bedminster, NJ, USA; and Northeastern University. He has contributed to O-RAN technical

specifications and submitted responses to multiple FCC and NTIA notice of inquiry and requests for comments. He is a co-PI in research projects on 6G funded by the U.S. NSF, OUDS, and NTIA. His research interests are in the analysis and development of protocols and architectures for future generations of cellular networks (5G and beyond). He received the several best paper awards and the 2022 Mario Gerla Award for Research in Computer Science. He is serving as the TPC Co-Chair for WNS3, from 2021 to 2022. He has organized the Open 5G Forum in Fall 2021 and the NextGenRAN Workshop at Globecom 2022. He is an Associate Technical Editor of IEEE Communications Magazine and a Guest Editor of IEEE JOURNAL ON SELECTED AREAS IN COMMUNICATIONS Special Issue on Open RAN.



Josep Miquel Jornet (Fellow, IEEE) received the degree in telecommunication engineering and the M.Sc. degree in information and communication technologies from Universitat Politecnica de Catalunya, Spain, in 2008, and the Ph.D. degree in electrical and computer engineering from the Georgia Institute of Technology, Atlanta, GA, USA, in August 2013. He is a Professor with the Department of Electrical and Computer Engineering, the Director of the Ultrabroadband Nanonetworking (UN) Laboratory, and the Associate Director of the

Institute for the Wireless Internet of Things, Northeastern University (NU). From August 2013 to August 2019, he was with the Department of Electrical Engineering, University at Buffalo (UB), The State University of New York

(SUNY). He is a leading expert in terahertz communications, in addition to wireless nano-bio-communication networks and the internet of nano-things. In these areas, he has coauthored more than 240 peer-reviewed scientific publications, including one book and granted five U.S. patents. His work has received over 15,500 citations (H-index of 56 as of September 2023). He is serving as the lead PI on multiple grants from U.S. federal agencies, including the National Science Foundation, the Air Force Office of Scientific Research, the Air Force Research Laboratory, and industry. He was a recipient of multiple awards, including the 2017 IEEE ComSoc Young Professional Best Innovation Award, the 2017 ACM NanoCom Outstanding Milestone Award, the NSF CAREER Award in 2019, the 2022 IEEE ComSoc RCC Early Achievement Award, and the 2022 IEEE Wireless Communications Technical Committee Outstanding Young Researcher Award, among others, and four best paper awards. He is the Editor-in-Chief of the Nano Communication Networks Journal (Elsevier) and an Editor of IEEE TRANSACTIONS ON COMMUNICATIONS and Nature Scientific Reports. He is an IEEE ComSoc Distinguished Lecturer (Class of 2022-2023, Extended to 2024).



Tommaso Melodia (Fellow, IEEE) received the Ph.D. degree in electrical and computer engineering from the Georgia Institute of Technology in 2007. He is the William Lincoln Smith Chair Professor with the Department of Electrical and Computer Engineering, Northeastern University, Boston. He is also the Founding Director of the Institute for the Wireless Internet of Things and the Director of Research for the PAWR Project Office. He is the Director of Research for the Platforms for Advanced Wireless Research (PAWR) Project Office, a 100*M*

public-private partnership to establish four city-scale platforms for wireless research to advance the U.S. wireless ecosystem in years to come. His research on modeling, optimization, and experimental evaluation of the Internet of Things and wireless networked systems has been funded by the National Science Foundation, the Air Force Research Laboratory the Office of Naval Research, DARPA, and the Army Research Laboratory. He is a Senior Member of ACM. He was a recipient of the National Science Foundation CAREER Award. He has served as the Technical Program Committee Chair for IEEE INFOCOM 2018; and the General Chair for IEEE SECON 2019, ACM Nanocom 2019, and ACM WUWnet 2014. He has served as an Associate Editor for IEEE TRANSACTIONS ON WIRELESS COMMUNICATIONS, IEEE TRANSACTIONS ON MOBILE COMPUTING, and Computer Networks (Elsevier), among others.



Michele Zorzi (Fellow, IEEE) received the Laurea and Ph.D. degrees in electrical engineering from the University of Padova, Italy, in 1990 and 1994, respectively. From 1992 to 1993, he was on leave with the University of California at San Diego (UCSD). In 1993, he joined the Faculty of the Dipartimento di Elettronica e Informazione, Politecnico di Milano, Italy. After spending three years with the Center for Wireless Communications, UCSD, he joined the School of Engineering, University of Ferrara, Italy, in 1998, where he became a Professor

in 2000. Since November 2003, he has been on the Faculty of the Information Engineering Department, University of Padova. His current research interests include performance evaluation in mobile communications systems, the Internet of Things, cognitive communications and networking, 5G mmWave cellular systems, vehicular networks, and underwater communications and networks. He has served as the Member-at-Large of the Board of Governors (2009-2011 and 2021-2023), the Director of Education (2014-2015), and the Director of Journals (2020-2021) with the IEEE Communications Society. He received several awards from the IEEE Communications Society, including the Best Tutorial Paper Award in 2008 and 2019, the Education Award in 2016, the Stephen O. Rice Best Paper Award in 2018, and the Joseph LoCicero Award for Exemplary Service to Publications in 2020. He was the Editor-in-Chief of IEEE Wireless Communications Magazine, (2003–2005), IEEE TRANSACTIONS ON COMMUNICATIONS (2008-2011), and IEEE TRANSACTIONS ON COGNITIVE COMMUNICATIONS AND NETWORKING (2014-2018).